Nanoscale mapping of the electron density at Al grain boundaries and correlation with grain-boundary energy

Proloy Nandi,[1,*] Xiahan Sang,[2,†] Eric R. Hoglund,[1,‡] Raymond R. Unocic,[2,§] Dmitri A. Molodov,[3,‖] and James M. Howe[1,¶]

[1]*Department of Materials Science & Engineering, University of Virginia, Charlottesville, Virginia 22904, USA*

[2]*Center for Nanophase Materials Sciences, Oak Ridge National Laboratory, Oak Ridge, Tennessee 37831, USA*

[3]*Institut für Metallkunde und Metallphysik, RWTH Aachen, Kopernikusstraße 1452056, Germany*

(Received 10 September 2018; published 16 May 2019)

Grain-boundary (GB) structures and energies are often calculated and have revealed correlations between the GB energy and change in electron density at the GB. In this work, the plasmon peak in valence electron energy-loss spectroscopy (VEELS) was used to determine the variation in electron density across four well-characterized GBs in Al, spanning a range of known GB energies. The results show that the plasmon energy is lower at the GB than in the adjacent grains due to a decrease in electron density, and the GB energy increases proportional to the density decrease. The decrease in electron density also extends further into adjacent grains with increasing GB energy, extending beyond the geometric changes, or physical width, revealed by electron microscopy. Plasmon damping also increases with increasing GB energy, indicative of increasing disruption of the electron density with increasing GB energy. These results demonstrate that VEELS can be a valuable tool for detecting small electron density changes at GBs, and this change clearly influences, and is correlated to, the GB energy.

DOI: 10.1103/PhysRevMaterials.3.053805

I. INTRODUCTION AND TEXT

The grain-boundary (GB) energy is an important parameter in determining the microstructure of materials, and determining the GB energy has been of great importance to the scientific community for decades [1–9]. Both experiments and computer simulations have been employed to calculate the GB energy and correlate this with the structure of the GB at the atomic level. Seeger and Schottky [10] first used the electron theory of metals to calculate the excess energy associated with GBs, assuming that the main contribution was electronic in origin. The average distances among atoms in the GB were considered to be somewhat larger, and the corresponding atomic density somewhat smaller, than in the ideal crystal. The displaced positive charge of the atom cores thus had to be screened by a redistribution of the conduction electrons, resulting in a lower electron density at the GB. This redistribution increases the energy in the GB and may be the dominant part of the GB energy. The basic ideas of Seeger and Schottky [10] were further developed and refined by other researchers, including Sutton and Balluffi [2], Smith and Ferrante [11], Wolf [12,13], Wright and Atlas [14], and others [15]. These studies show that there is a correlation between the electron density at the GB and the GB energy, but it is still not clear how much the change in electron density contributes to the energy and how this varies with the atomic structure of different GBs.

Valence electron energy-loss spectroscopy (VEELS) records the energy lost by an incident electron due to the excitations of outer-shell electrons in the low-energy-loss range (0–50 eV), and it is highly sensitive to the electron states that are responsible for the intrinsic properties of materials [16]. One of the main inelastic scattering processes that occur in this range is the generation of quantized high-frequency ($\sim 10^{16}$ Hz) longitudinal electron excitations known as volume plasmons [17,18]. Collective oscillations of the valence electrons occur at a resonance angular frequency:

$$\omega_p = \{ne^2/\varepsilon_0 m\}^{1/2}, \tag{1}$$

where n is the valence electron density, e is the electron charge, ε_0 is the permittivity of vacuum, and m is the electron mass. The plasmon energy, E_p, can be correlated with the valence electron density n, since E_p is given by

$$E_p \cong \hbar\omega_p = \hbar\left[\frac{ne^2}{\varepsilon_0 m}\right]^{1/2}, \tag{2}$$

where $\hbar$ is Planck's constant h divided by 2π. The full width at half maximum of the peak produced by the plasma resonance is equivalent to dampening, Γ, which is an inverse lifetime [17,18]. Hence, by measuring the plasmon resonance from the GB and adjacent grains, it should be possible to determine the difference in electron density and dampening behavior at the GB. In the present work, we use spatially resolved VEELS to investigate symmetric tilt and tilt-twist GBs in Al bicrystals with known energies, to obtain fundamental insight into the variation in valence electron density across the GB and its relationship with GB energy. Al was chosen as a model

*alloynandi@gmail.com
†sangx@ornl.gov
‡erh3cq@virginia.edu
§unocicrr@ornl.gov
‖Molodov@imm.rwth-aachen.de
¶Corresponding author: jh9s@virginia.edu

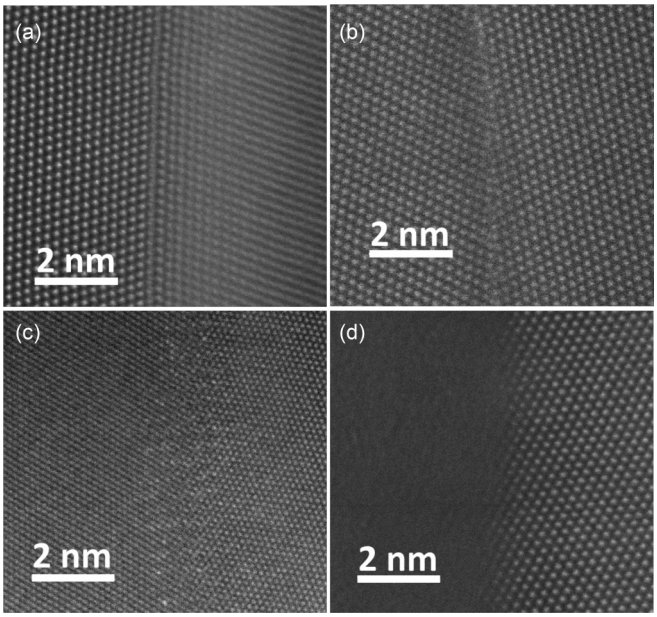

FIG. 1. High-resolution STEM images of all four GBs in an edge-on position: (a) GB 1, (b) GB 4, (c) GB 3, and (d) GB 2.

metal system to avoid complications associated with VEELS analysis of materials such as oxide ceramics.

High-resolution scanning transmission electron microscope (STEM) images of the four GBs studied in the VEELS experiments are shown in an edge-on orientation in Fig. 1, where the general structures of the GBs are clearly visible. GB 1, GB 3, and GB 4 are symmetric tilt boundaries with the tilt axis being ⟨110⟩, ⟨111⟩, and ⟨110⟩, respectively, while GB2 is a tilt-twist boundary with the tilt axis being ⟨100⟩. Features and energies of the four GBs are given below, and additional information is provided in the Supplemental Material [19].

GB 1: 70.8°[110] tilt (relatively low energy ∼60–80 mJ/m^2, close to a coherent twin Σ3 (111) GB [6,8]).

GB 2: Mixed 20.9°[100] (twist component $\xi = 21^\circ$) tilt/twist GB (relatively high energy ∼560–580 mJ/m^2 [20]).

GB 3: 38.7°[111] tilt (medium energy GB ∼450–470 mJ/m^2, close to Σ7 (231) [6,20]).

GB 4: 52.7°[110] tilt (medium energy GB ∼380–400 mJ/m^2, close to Σ11 (332) [6,15,21]).

Spectrum images (SIs) acquired across the GBs (see Supplemental Fig. S2 [19] and Methods section for details) showed a shift in the first plasmon peak positions toward lower energy at the GBs. To visualize the shift in plasmon peak position, ΔE_p, for the various GBs, plasmon peaks from the

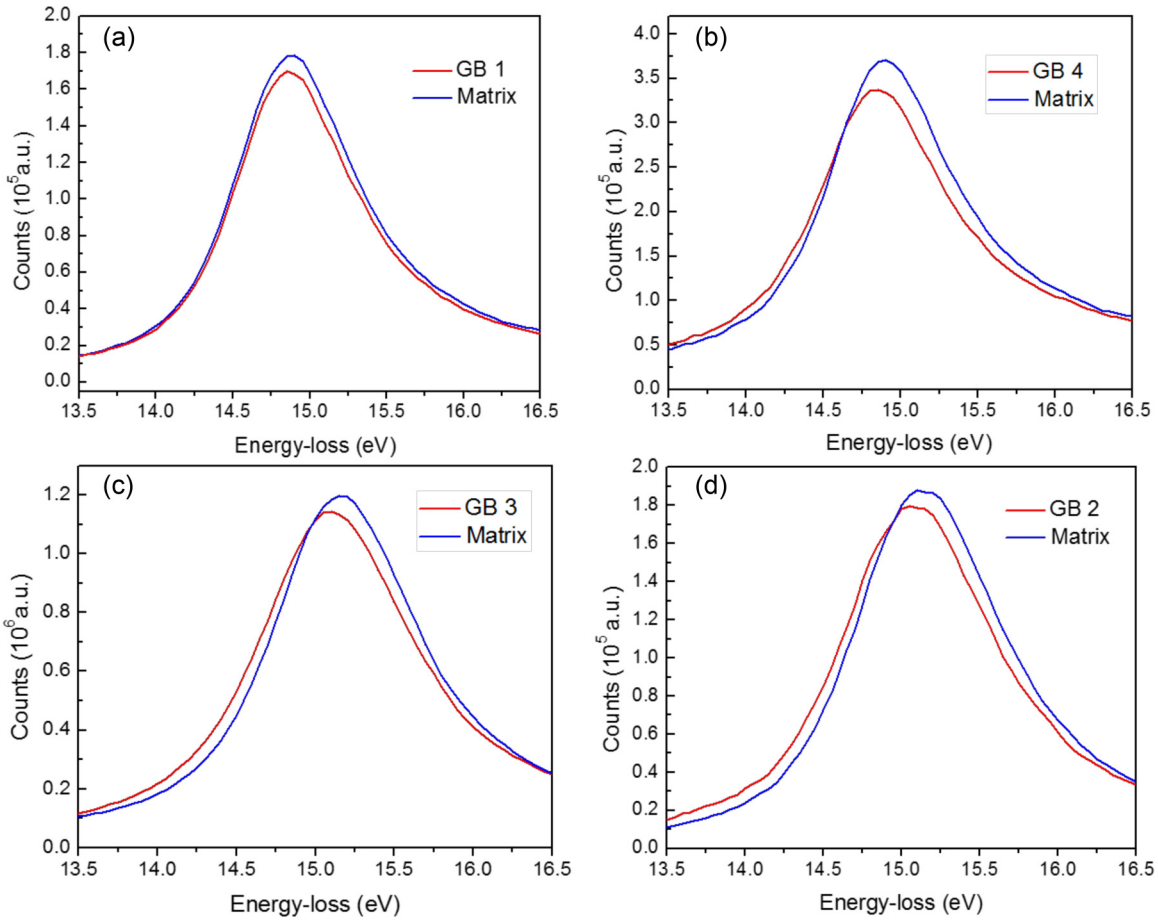

FIG. 2. (a–d) Plasmon peaks from the low-loss spectra acquired from the GBs and adjacent grains (matrix) overlaid to reveal the increasing peak shifts toward lower energy with increasing GB energy.

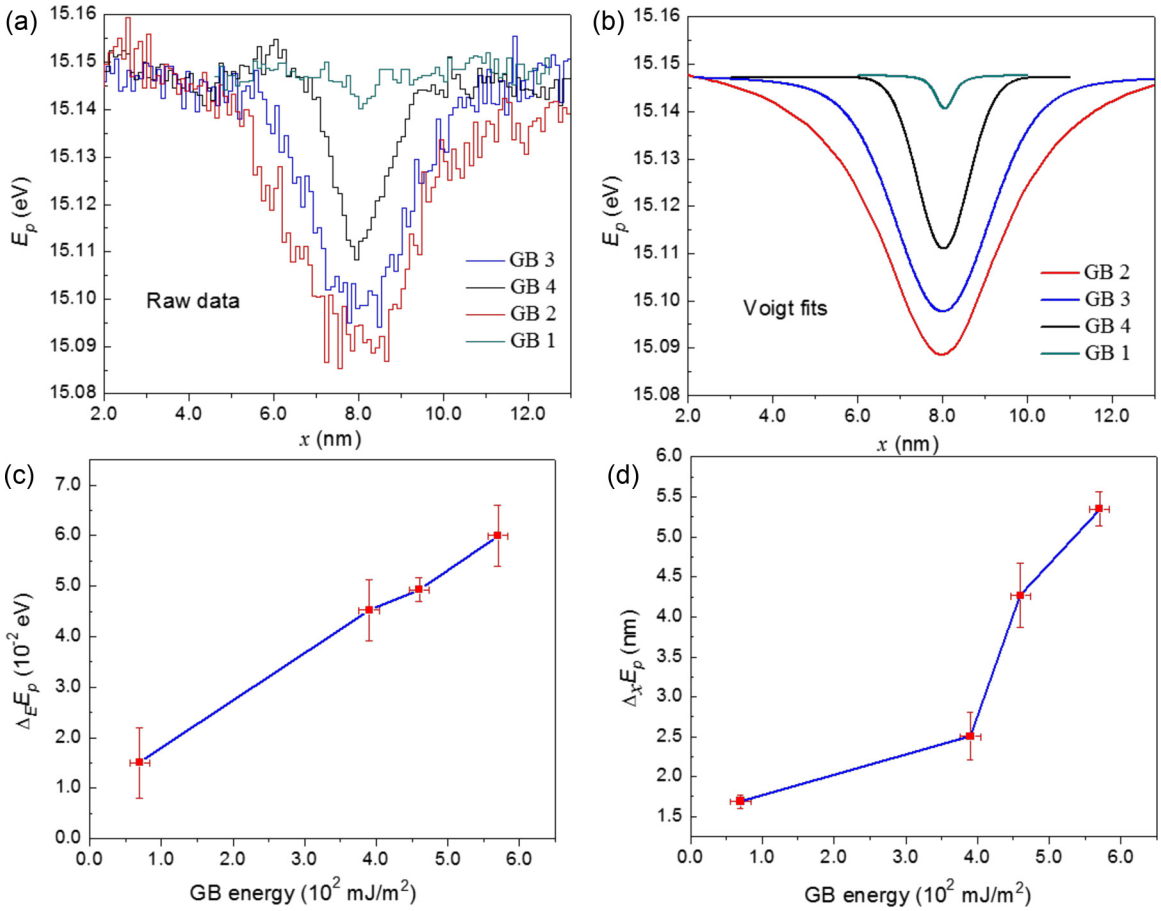

FIG. 3. (a) Comparison of raw plasmon energy profiles experimentally obtained across all four GBs. (b) The Voigt fits, which depict the change in $\Delta_E E_p$ and $\Delta_x E_p$ for the GBs. (c) Variation of $\Delta_E E_p$ as a function of GB energy. (d) Dependence of $\Delta_x E_p$ with GB energy.

low-loss spectra acquired from the adjacent grains and GB were overlaid, as shown in Fig. 2. Spectra from the grains and GB were normalized with respect to the zero-loss peak (ZLP) to account for variations in experimental conditions during acquisition. A decrease in intensity accompanied by a shift in the plasmon peak position toward lower energy was observed for all GBs in Fig. 2. A loss of intensity in the bulk plasmon is attributed to the *begrenzungs* effect, where intensity is taken out of the bulk plasmon to create the component associated with the interface/GB [22]. To ensure the plasmon peak shifts were not due to a variation in thickness at the GBs (e.g., due to GB grooving [23,24]), thickness maps were calculated (see Supplemental Fig. S4 [19] for details).

The plasmon energy profiles (raw data) from all four GBs are shown in Fig. 3(a) in the same graph for comparison. (Strictly speaking, the plasmon peak position and the plasmon energy E_p are not the same, but for Al where plasmon dampening is small, the difference between these two quantities is negligible [17].) Plasmon damping Γ at the GBs was found to increase by ∼0.05–0.08 eV, depending on the GB structure. To better depict the difference in plasmon energy, $\Delta_E E_p$, and the distance that E_p varies into the grains, $\Delta_x E_p$, individual profiles for the four GBs were fitted with a Voigt function (see Supplemental Fig. S3(b) [19]) and Fig. 3(b) compares the resulting Voigt function fits. It can be seen that $\Delta_E E_p$ and $\Delta_x E_p$ both increase with increasing GB energy. Figure 3(c) shows a plot of $\Delta_E E_p$ vs GB energy and this graph clearly shows that $\Delta_E E_p$ increases proportional to (almost linearly) the GB energy. The measured $\Delta_x E_p$ were plotted as a function of GB energy and these also increase with GB energy, as shown in Fig. 3(d), although not as regularly as $\Delta_E E_p$.

Since E_p is proportional to $\sqrt{n}$ [Eq. (2)], the decrease in $\Delta_E E_p$ provides information about the decrease in local electron density at the GB. As shown in Fig. 3(c), $\Delta_E E_p$ increases with increasing GB energy, indicating that the local electron density decreases proportionally. Wright and Atlas [14] used density-function theory (DFT) to calculate the electron density distributions at $\Sigma 11$ and $\Sigma 3$ twin boundaries in Al. For a $\Sigma 11$ (113) boundary, their model predicts a 10% reduction in the average electron density at the GB compared to the bulk, and this lower density extends three atomic layers into the grains on either side of the GB. Figures 3(a) and 3(b) demonstrate that this lowering of the electron density at the GB was revealed by the incident STEM probe through a local change in E_p [or ω_p in Eqs. (1) and (2)], and that the width of the electron deficit region extends into the matrix on either side of the GBs. However, the results from GB 4, which is close to a $\Sigma 11$ ($\bar{3}32$) with an energy of 380–400 mJ/m^2, shows a plasmon peak shift of $\Delta_E E_p \approx 0.045$ eV, which only corresponds to a 0.53% decrease in electron density as calculated from Eq. (2). The reason for this lower value compared to Wright and Atlas [14] is likely due to delocalization effects

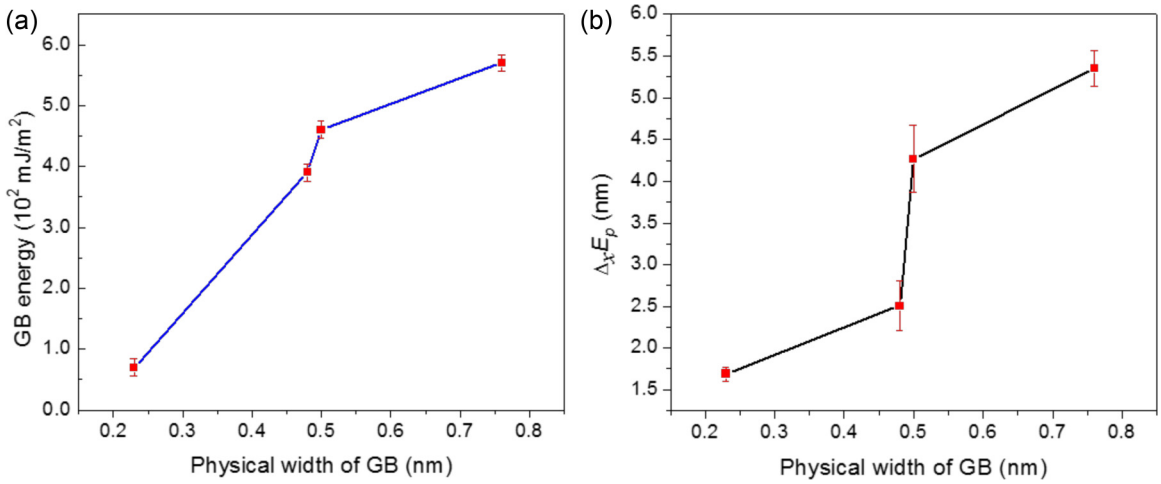

FIG. 4. (a) Plot of GB energy vs physical width (measured from high-resolution STEM images). (b) Plot of measured $\Delta_x E_p$ as a function of GB physical width.

that convolute the GB VEELS signal with the matrix signal, as discussed further below.

An experimental estimate of the delocalization diameter (i.e., the effective diameter giving rise to the VEELS signal), can be made from the line scan across GB 1, a $\Sigma 3$ GB, which is atomically sharp and flat, as shown in the STEM images in Fig. S5(a) [19] and Fig. 1(a). The width of the GB is about one interplanar spacing (0.23 nm) and has a corresponding $\Delta_x E_p$ of $\sim$1.7 nm in Fig. 3(d). Since the electron probe diameter is 0.12 nm, this results in a delocalization diameter of approximately 1.7–0.23 nm $\approx$ 1.5 nm. The delocalization distance for valence electron scattering can be estimated using the following expression for L_{50}, the length containing 50% of the inelastic scattering: $L_{50} = 0.52\lambda/\langle\theta\rangle$ [25,26], where $\langle\theta\rangle$ is the median scattering angle. For 15 eV energy loss and 200-keV incident electrons, this equation gives a delocalization distance of $\sim$2 nm, which is in reasonable agreement with the present experimental value of 1.5 nm. This experimentally determined delocalization diameter can be used to deduce the actual $\Delta_x E_p$ in the absence of delocalization, as described below.

The measured $\Delta_x E_p$ for GB 4 in Fig. 3(d) is 2.5 ± 0.3 nm. Taking the effective delocalization diameter to be 1.5 nm, the actual $\Delta_x E_p$ is 1.0 ± 0.3 nm, which is almost twice that of the measured width of 0.48 nm for GB 4 from the STEM image in Fig. S5(b) [19]. This leads to the important result that the decrease in electron density at the GB extends over twice the distance of atomic displacements visible at the GB in high-resolution STEM images (see Supplemental Fig. S5 [19]), which give an estimate of the physical width (thickness) of the boundary. In other words, the decrease in electron density spreads smoothly over —two to three {111} atomic planes on either side of the GB plane, beyond the observed physical width. Figure 4(a) shows that this description applies to the other GBs, where the electron density deficit extends further into the adjacent grains with increasing GB energy. For GB 2 with the highest energy, the decreased electron density extends up to 1.93 ± 0.2 nm on either side of the GB, while the physical width of the GB in the STEM image is only about 0.76 nm.

Comparing the measured $\Delta_x E_p$ with the physical width of the GBs in Fig. 4(b) also shows an increasing trend, although not as regular as the GB energy in Fig. 4(a). This is because GB 4 and GB 3 have a difference in energy of only $\sim$50–70 mJ/m^2 (i.e., 380–400 mJ/m^2 vs 450–480 mJ/m^2) and their physical widths are comparable, but the measured $\Delta_x E_p$ in Fig. 4(b) indicate that GB 3 has a significantly wider region of lower electron density compared to GB 4. The plasmon peak shift, $\Delta_E E_p$, for GB 3 is higher than GB 4 by $\sim$0.005–0.01 eV, as shown in Fig. 3(c), further indicating a greater electron density deficit. While GB 1 and GB 2 behave as expected in comparison with GB energy in Fig. 4(a), the reason why GB 4 and GB 3 behave differently may be because they are $\langle 110\rangle$ and $\langle 111\rangle$ tilt boundaries, respectively, so the detailed way in which the electron density deficit redistributes across the planes parallel to these GBs varies with the different tilt axes. Note that it is also possible that the plasmon dispersion, i.e., variation in plasmon energy E_p with wave vector $\boldsymbol{q}$, could change at the GB and influence the results [17,18]. In this study though, the probe convergence angle and collection angles were both relatively large and a 2-mm entrance aperture was used, so the plasmon dispersion is weighted such that the intensity near $\boldsymbol{q} = 0$ is largest. This in combination with the combined volume plasmon (VP) and VP + quasielastic scattering would make the sensitivity to dispersion small. This argument does not hold for nonzero $\boldsymbol{q}$, or when the convergence is small relative to the collection angle. When either of these scenarios hold then modifications of the aluminum VPs' dispersion or existence of new interface modes would contribute to shifts in the apparent VP maximum. It could lead to some of the variation, i.e., spread, in our results. In summary, these results conclusively demonstrate that the deficit in valence electron density at the GB increases and extends further into the adjacent matrix grains with increasing GB energy, and that this electronic width of the GB is larger than the physically defined GB width from STEM images.

Van Benthem *et al.* [27] reported variations in the index of refraction across $\Sigma 5$ and $\Sigma 13$ GBs of Fe-doped $SrTiO_3$ using spatially resolved EELS. The authors calculated the

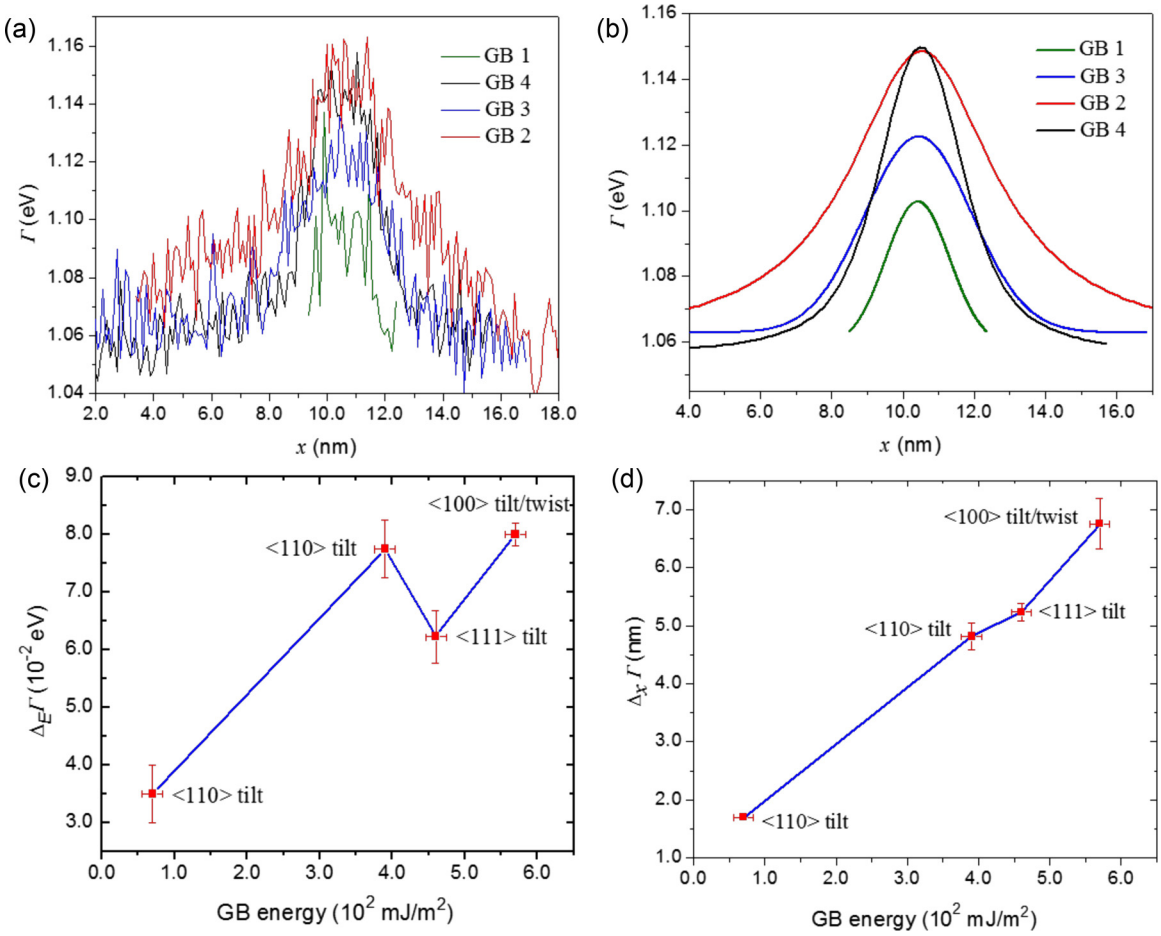

FIG. 5. (a) Comparison of Γ profiles across all four GBs. (b) The Voigt fits, which depict the changes in $\Delta_E\Gamma$ and $\Delta_x\Gamma$ for the four GBs. (c) Plot of $\Delta_E\Gamma$ as a function of GB energy. (d) Variation in measured $\Delta_x\Gamma$ as a function of GB energy.

electron density difference between the matrix and GB core, concluding that the Σ13 GB had a larger deficiency than the Σ5 and the density difference was attributed to O vacancy formation. The widths of a plot of the refractive index across the Σ5 and Σ13 GBs in that study were ∼5 and ∼13 nm, respectively, which are considerably greater than the present Σ3 and Σ11 GB widths of 1.7 and 2.5 nm, respectively, and this may be partly because $SrTiO_3$ is an oxide, and it allows for a longer-range variation in potential than a metal like Al. Müllejans and French [28] also performed a detailed VEELS analysis of a near Σ11 tilt GB in α-Al_2O_3 to compare the electron states and various interband transitions with those of bulk material. This paper was mainly concerned with developing low-loss EELS as a quantitative technique to understand the electronic states at an oxide GB and made no connection to GB energy.

The Γ (plasmon damping) profiles across the four GBs are shown in Fig. 5(a). Similar to the previous plasmon energy profiles, a Voigt function gave a reasonably good fit to the Γ profiles and these are shown separately in Fig. 5(b). Measurement of the magnitude ($\Delta_E\Gamma$) and spatial extent ($\Delta_x\Gamma$) of Γ is further described in Supplemental Fig. S3(c) [19]. Plasmons at a GB are expected to have a shorter lifetime compared to the bulk due to additional electron scattering from the less-ordered structure, and hence, Γ is expected to increase at a GB. A $\Delta_E\Gamma$ of 0.035 ± 0.005 eV was observed for the Σ3 GB 1, which contains no dislocations, indicating that plasmons are highly sensitive to small changes in planar stacking and electron density at a GB. The damping of plasmons and corresponding $\Delta_E\Gamma$ were found to increase from GB 1 to GB 4 and at the other GBs, as shown in Fig. 5(c). Unlike the plasmon peak shifts in Fig. 3(c), $\Delta_E\Gamma$ was not found to increase proportionally to the GB energy, as shown in Fig. 5(c). Different values of $\Delta_E\Gamma$ for the GBs are expected to result from differences in their geometry and structure, and $\Delta_E\Gamma$ for GB 3 may be less than expected because it is close to a Σ7 symmetric tilt GB. Figure 5(d) shows that $\Delta_x\Gamma$ also increases regularly with increasing GB energy, further indicating that the electron density deficit expands into the surrounding grains with increasing GB energy.

In conclusion, these studies demonstrate that it is possible to directly measure the change in electron density at a GB with nanometer spatial resolution even for the lowest possible GB energies (e.g., Σ3). Low-loss spectra acquired from the four GBs showed an increase in plasmon peak shift toward lower energy with increasing GB energy, making it is possible to conclude that increasing GB energy is clearly correlated with decreasing valence electron density at a GB. The electron density deficit also extends further into the matrix with increasing GB energy and appears to be significantly wider than the regions of atomic displacements visible in high-resolution STEM images of GBs. The magnitude and spatial extent of

plasmon damping were found to increase with increasing GB energy, demonstrating that GB electrons have shorter lifetimes compared to electrons in the bulk, and presumably correlated with increased scattering due to increasing GB disorder. The results of this investigation support the original ideas of Seeger and Schottky [10] about the origin of the GB energy, and they also add considerable insight into the properties of electrons at GBs in metals.

II. METHODS

A. TEM sample preparation

Four bicrystals of 99.999% pure Al with well-characterized GBs were studied, as described previously and shown in Fig. S1 in the Supplemental Material [19]. The bicrystals were cut perpendicular to the GB using a slow-speed saw to produce 1-mm-thick slices. The slices were mechanically polished to 120 μm and punched to obtain 3-mm disks. The disks were dimpled to 20–30 μm thickness at the center on the GB and electropolished to perforation using a 25 vol % nitric acid/75 vol % methanol solution at 22 V at –40 °C. EEL spectra were collected from the GBs in the electropolished foils keeping them nearly edge on, as shown in Fig. S1 [19].

B. VEELS in STEM

Two different STEMs were used for the VEELS experiments: (1) a Nion UltraSTEM 100 at Oak Ridge National Laboratory (ORNL) [29] operating at 100 keV with a cold field-emission gun (CFEG) and energy spread of 0.55 eV, and (2) a Hitachi HD2700C at Brookhaven National Laboratory (BNL) [30] with a CFEG operating at 200 keV with an energy spread of 0.35 eV. Other important specifications and conditions used are given in Table 1 in the Supplemental Material [19].

C. Data acquisition and analysis

Line scans were acquired across the GBs for the VEELS experiments. A scan length of 15 nm was selected (red line in Fig. S2 [19]) to obtain EEL spectra from the adjacent grains without delocalization effects from the GB. Spectrum images (SIs) were obtained using point-by-point EEL spectra acquisition with a step increment of 0.1 nm and a dwell time of 0.1 s/pixel to obtain good signal to noise in the SI. EEL spectra up to 50 eV were collected using a Gatan Enfina spectrometer.

Individual spectra in the SI were aligned with respect to the zero-loss peak (ZLP) to an accuracy of 0.05 eV (1 pixel) using a built-in routine in DIGITAL MICROGRAPH^{TM} software. Plasmon peaks from individual spectra were fitted with a Gaussian function, which gave the plasmon peak position profile and full width half maximum (FWHM) profile along the entire scan length. The FWHM is equivalent to Γ, and the plasmon peak position is approximately equal to E_p when Γ is small. Since plasmons peaks are asymmetric due to a contribution from a range of scattering vectors [31], fitting errors were minimized by fitting each plasmon peak separately with two Gaussian curves, one with respect to the peak position (maximum amplitude) and a second with respect to the FWHM. The former gave the E_p profile and the latter gave the Γ profile along the line scan.

ACKNOWLEDGMENTS

J.M.H., P.N., and E.R.H. are grateful for funding under NSF Grant No. DMR-1106230 and the VPR Office at UVA. The authors thank Dr. Eric Stach and Dr. Dong Su for help with research conducted in part at CFN-BNL supported by the U.S. DOE-BES under Contract No. DE-SC-00112704, and acknowledge research supported as part of a user proposal at ORNL-CNMS, which is a U.S. DOE Office of Science User Facility (X.S. and R.R.U.).

All authors contributed to the intellectual merit and preparation of the manuscript. Additionally, P.N. performed the main body of experimental work and analysis, D.A.M. provided the bicrystal samples, R.R.U. and X.S. facilitated STEM analyses at ORNL, E.R.H. contributed to the plasmon analysis, and J.M.H. was the principal investigator on the project.

The authors declare that they have no competing interests in this article.

[1] F. J. Humphreys and M. Hatherly, *Recrystallization and Related Annealing Phenomena* (Elsevier, Amsterdam, 2004).

[2] A. P. Sutton and R. W. Balluffi, *Interfaces in Crystalline Materials* (Clarendon, Oxford, 1996).

[3] G. Gottstein and L. Shvindlerman, *Grain Boundary Migration in Metals* (CRC Press, Boca Raton, FL, 2009).

[4] D. L. Olmsted, E. A. Holm, and S. M. Foiles, Survey of computed grain boundary properties in face-centered cubic metals—II: Grain boundary mobility, Acta Mater. **57**, 3704 (2009).

[5] H. Gleiter, On the structure of grain boundaries in metals, Mater. Sci. Eng. **52**, 91 (1982).

[6] D. L. Olmsted, S. M. Foiles, and E. A. Holm, Survey of computed grain boundary properties in face-centered cubic metals: I. Grain boundary energy, Acta Mater. **57**, 3694 (2009).

[7] G. S. Rohrer, E. A. Holm, A. D. Rollett, S. M. Foiles, J. Li, and D. L. Olmsted, Comparing calculated and measured grain boundary energies in nickel, Acta Mater. **58**, 5063 (2010).

[8] D. M. Saylor, B. S. El Dasher, A. D. Rollett, and G. S. Rohrer, Distribution of grain boundaries in aluminum as a function of five macroscopic parameters, Acta Mater. **52**, 3649 (2004).

[9] G. S. Rohrer, D. M. Saylor, B. El Dasher, B. L. Adams, A. D. Rollett, and P. Wynblatt, The distribution of internal interfaces in polycrystals, Z. Metallkd. **95**, 197 (2004).

[10] A. Seeger and G. Schottky, Die energie und der elektrische widerstand von grosswinkelkorngrenzen in metallen, Acta Metall. **7**, 495 (1959).

[11] J. R. Smith and J. Ferrante, Grain-boundary energies in metals from local-electron-density distributions, Phys. Rev. B **34**, 2238 (1986).

[12] D. Wolf, Correlation between energy and volume expansion for grain boundaries in fcc metals, Scr. Metall. **23**, 1913 (1989).

[13] D. Wolf, Structure-energy correlation for grain boundaries in F.C.C. metals—I. Boundaries on the (111) and (100) planes, Acta Metall. **37**, 1983 (1989).

[14] A. F. Wright and S. R. Atlas, Density-functional calculations for grain boundaries in aluminum, Phys. Rev. B **50**, 15248 (1994).

[15] T. Uesugi and K. Higashi, First-principles calculation of grain boundary energy and grain boundary excess free volume in aluminum: role of grain boundary elastic energy, J. Mater. Sci. **46**, 4199 (2011).

[16] J. M. Howe and V. P. Oleshko, Application of valence electron energy-loss spectroscopy and plasmon energy mapping for determining material properties at the nanoscale, J. Electron Microsc. (Tokyo) **53**, 339 (2004).

[17] R. F. Egerton, *Electron Energy-Loss Spectroscopy in the Electron Microscope* (Springer Science & Business Media, Berlin, 2011).

[18] H. Raether, *Excitation of Plasmons and Interband Transitions by Electrons*, Springer Tracts in Modern Physics Vol. 88 (Springer-Verlag, Berlin, 1980).

[19] See Supplemental Material at http://link.aps.org/supplemental/10.1103/PhysRevMaterials.3.053805 for further details regarding regarding the crystallography of the GBs, the STEM experiments, extraction of GB EELS data, and HRTEM measurements of GB width.

[20] D. A. Molodov, L. A. Barrales-Mora, and J.-E. Brandenburg, Grain boundary motion and grain rotation in aluminum bicrystals: recent experiments and simulations, IOP Conf. Ser.: Mater. Sci. Eng. **89**, 012008 (2015).

[21] A. Suzuki and Y. Mishin, Interaction of point defects with grain boundaries in fcc metals, Interface Sci. **11**, 425 (2003).

[22] A. Howie, Interpretation of spatially resolved valence loss spectra, in *Topics in Electron Diffraction and Microscopy of Materials*, edited by P. B. Hirsch, Microscopy in Materials Science Series (IOP Publishing, London, 1999), pp. 79–108.

[23] W. W. Mullins, The effect of thermal grooving on grain boundary motion, Acta Metall. **6**, 414 (1958).

[24] W. W. Mullins and P. G. Shewmon, The kinetics of grain boundary grooving in copper, Acta Metall. **7**, 163 (1959).

[25] R. F. Egerton, Scattering delocalization and radiation damage in STEM-EELS, Ultramicroscopy **180**, 115 (2017).

[26] R. F. Egerton, Limits to the spatial, energy and momentum resolution of electron energy-loss spectroscopy, Ultramicroscopy **107**, 575 (2007).

[27] K. van Benthem, G. Tan, L. K. DeNoyer, R. H. French, and M. Rühle, Local Optical Properties, Electron Densities, and London Dispersion Energies of Atomically Structured Grain Boundaries, Phys. Rev. Lett. **93**, 227201 (2004).

[28] H. Müllejans and R. H. French, Interband electronic structure of a near-$\Sigma 11$ grain boundary in α-alumina determined by spatially resolved valence electron energy-loss spectroscopy, J. Phys. D: Appl. Phys. **29**, 1751 (1996).

[29] O. L. Krivanek, G. J. Corbin, N. Dellby, B. F. Elston, R. J. Keyse, M. F. Murfitt, C. S. Own, Z. S. Szilagyi, and J. W. Woodruff, An electron microscope for the aberration-corrected era, Ultramicroscopy **108**, 179 (2008).

[30] H. Inada, L. Wu, J. Wall, D. Su, and Y. Zhu, Performance and image analysis of the aberration-corrected Hitachi HD-2700C STEM, J. Electron Microsc. (Tokyo). **58**, 111 (2009).

[31] P. Moreau, N. Brun, C. A. Walsh, C. Colliex, and A. Howie, Relativistic effects in electron-energy-loss-spectroscopy observations of the Si/SiO_2 interface plasmon peak, Phys. Rev. B **56**, 6774 (1997).